J Appl Electrochem (2014) 44:1013–1023
DOI 10.1007/s10800-014-0723-x

RESEARCH ARTICLE

Numerical modeling and experimental validation of pouch-type lithium-ion battery

Jung-Hoon Song · Seung-Jae You · Dong Hyup Jeon

Received: 22 May 2014 / Accepted: 27 July 2014 / Published online: 14 August 2014

Abstract The thermal behavior of pouch-type lithium-ion batteries during discharge and charge cycles is investigated by numerical simulation. A transient thermal model using finite element method software is developed through the modification of an electrochemical-thermal model. The developed model is validated with experimental data. For the experiment, a 304252 pouch cell is fabricated and tested in the laboratory. This model captures the dynamic responses of temperature, and distributions of current density and temperature, during discharge and charge cycles. Our results indicate that the discharge temperature is higher than the charge temperature at cut-off voltage. The temperature distribution upon discharge is similar to that of charge. On the other hand, different temperature distributions are observed at various C rates. The temperature profiles obtained from modeling and experiment are in good agreement.

Keywords Pouch type Li-ion battery · Thermal model · Validation · Temperature distribution · Discharge and charge

List of symbols

c	Lithium concentration (mol $L^{-1)}$
C_p	Heat capacity (J kg^{-1} K^{-1})
D	Diffusion coefficient (m^2 s^{-1})
F	Faraday constant (96,485 C mol^{-1})
ΔH	Enthalpy change of chemical reaction (J mol^{-1})
h	Heat transfer coefficient (W m^{-2} K^{-1})
i	Current density (A m^{-2})
I	Applied current (A)
k	Charge-transfer rate coefficient [A m^{-2} (m^3 mol^{-1})$^{2/3}$]
L	Thickness (m)
n	Charge number pertaining to the reaction
$\dot{q}$	Heat generation per unit volume (W m^{-3})
r_p	Radius of electrode particles (m)
r	Rate of reaction (mol s^{-1})
R	Electrical resistance (Ω m)
ΔS	Entropy change (J mol^{-1} K^{-1})
t	Time (sec)
T	Temperature (K)
V	Voltage (V)
V^o	Open circuit voltage (V)
x	Li content in $Li_xMn_2O_4$
y	Li content in Li_yC_6

Greek letters

ε	Volume fraction
φ	Electrical potential (V)
κ	Thermal conductivity (W m^{-1} K^{-1})
σ	Electrical conductivity (S m^{-1})
ρ	Density (kg m^{-3})
υ	Volume (m^3)

Subscripts and superscripts

1	Electronic (solid) phase
2	Ionic (liquid) phase
PCC	Positive current collector
PE	Positive electrode
NCC	Negative current collector

J.-H. Song · S.-J. You
Secondary Battery Research Team, Research Institute of Industrial Science and Technology, Pohang 790-330, Republic of Korea

D. H. Jeon (✉)
Department of Mechanical System Engineering, Dongguk University-Gyeongju, 123 Dongdae-ro, Gyeongju, Gyeongsangbuk-do 780-714, Republic of Korea
e-mail: jeondh@dongguk.ac.kr

NE Negative electrode
Max Maximum

1 Introduction

Lithium-ion (Li-ion) batteries are widely used as power sources in products ranging from portable devices to hybrid electric vehicles (HEVs), and have received much attention as key devices for electric vehicles (EVs) and energy storage systems (ESSs). Such applications require the scale-up of commercial Li-ion batteries. As the battery size increases, its heat generation increases, leading to a temperature rise and non-uniform temperature distribution in the battery. The high temperature can deteriorate cell performance and the possibility exists that temperature non-uniformity induces partial degradation in the battery. This may result in a serious safety problem. As a result, thermal management becomes the key factor affecting battery cycle life and safety.

To define and optimize a thermal management system, it is necessary to understand the thermal behavior of batteries. There have been many previous works in the area of thermal management of Li-ion batteries based on numerical modeling and experiment. Early studies of battery thermal management focused on a fundamental understanding of battery prototypes with numerical models [1–6]. Recently, researchers have conducted numerical simulations combined with experiments on commercial-scale Li-ion batteries [7–17]. In most of these studies, a thermal model is coupled with three different approaches to characterize the thermal behavior of a battery: a semi-empirical model, an equivalent circuit model, and an electrochemical model. The first two models describe thermal behavior while ignoring the detailed physics of electrochemistry that includes distribution of electronic and ionic currents and depending temperature contour [16]. On the other hand, a coupled electrochemical-thermal model accounts for the thermal behavior of a battery, and provides insight into electrochemical phenomena. This model is well suited for battery component design by providing detailed information about electrochemical behavior. However it is not compatible with full cell-scale battery design for thermal management purposes due to its high computational cost [11]. We therefore developed a simplified and computationally efficient thermal model that can be used to estimate the internal temperature of the battery.

In this study, the thermal behavior of a pouch-type Li-ion battery is investigated. A transient three-dimensional model is incorporated with finite element method (FEM) simulation. To limit the computing time for the thermal analysis, a mathematical reduction of a complex electrochemical-thermal model has led to the development of simplified thermal model in this study. Since the major issues in thermal modeling of Li-ion batteries are exothermic and endothermic heat generation due to entropy change, these are calculated at the heat source term using experimental data. Although Li-polymer batteries (LIPBs) are currently one of the most popular applications in EVs and HEVs, few studies have been reported in the literature on thermal behavior of pouch cell. In addition, there are few reports in the literature on the thermal analysis of Li-ion batteries during charging, even though rapid charging of EV and HEV batteries has attracted much attention recently. Therefore, we conducted thermal modeling on the discharge and charge of this type of battery. To determine the reliability of the proposed model, the simulated results are compared with the measured battery temperature. Consequently, the goals are to understand the thermal behavior of a pouch-type Li-ion battery and validate the developed thermal model.

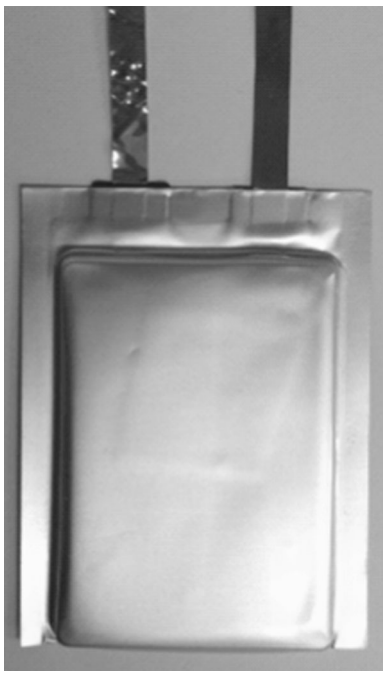

Fig. 1 Pouch type Li-ion battery

2 Experiment

2.1 Cell fabrication

A 304252 pouch cell with 0.23 Ah capacity is fabricated in the laboratory, as shown in Fig. 1. The cell is comprised of repeating units of porous positive and negative electrodes with current collectors, an electrolyte of 1 M $LiPF_6$ in 1:1 ethylene carbonate (EC):dimethyl carbonate (DMC), and a

porous polyethylene (PE) separator. The positive electrode consists of 94 wt% $LiMn_2O_4$ (LMO) mixed with 3 wt% carbon black and 3 wt% polyvinylidene difluoride (PVdF). The negative electrode consists of 94 wt% artificial graphite mixed with 1 wt% carbon and 5 wt% styrene-butadiene rubber (SBR). Aluminum and copper foils were used as the positive and negative current collectors, respectively. The cathode (i.e., the positive electrode was coated on both sides of the aluminum foil) and the anode (i.e., the negative electrode was coated on both sides of the copper foil) were stacked in the polypropylene-coated aluminum pouch. The cathode and anode were separated by a porous separator. A positive tab was welded on the positive current collector and a negative tab was welded on the negative current collector using a resistance welder. Aluminum and nickel were used as the positive and negative tabs, respectively.

2.2 Temperature measurement

A temperature measurement was conducted on an LMO/graphite Li-ion battery. Figure 2a shows the experimental devices used to measure the thermal behavior of the 304252 pouch cell during discharge and charge cycles. The experiment was conducted in a laboratory where a constant ambient temperature was kept. A schematic diagram of the experimental setup is shown in Fig. 2b. The cell was charged and discharged on a battery test station (model 4600A, Maccor). The surface temperature was recorded using a calibrated thermal data logger (model 51101C, Chroma). To keep the cell away from the external heat sources, it was placed in a chamber in which a constant temperature of 24.5 °C was maintained during the test. The cell was equipped with K-type thermocouples. The battery test station, chamber and data logger were connected to a personal computer to control and record the applied current, output voltage, and temperature. A constant-current-constant-voltage (CCCV) protocol for both the charge and discharge cycles was used until reaching a cut-off voltage (4.2 V for charge and 3.0 V for discharge). A rest time between the charge and discharge was given to relax and stabilize the voltage and the temperature of the cell.

3 Model development

3.1 Thermal model

A transient thermal model is developed to solve the energy equation using commercial finite element analysis (FEA) software. The energy balance equation can be written as follows.

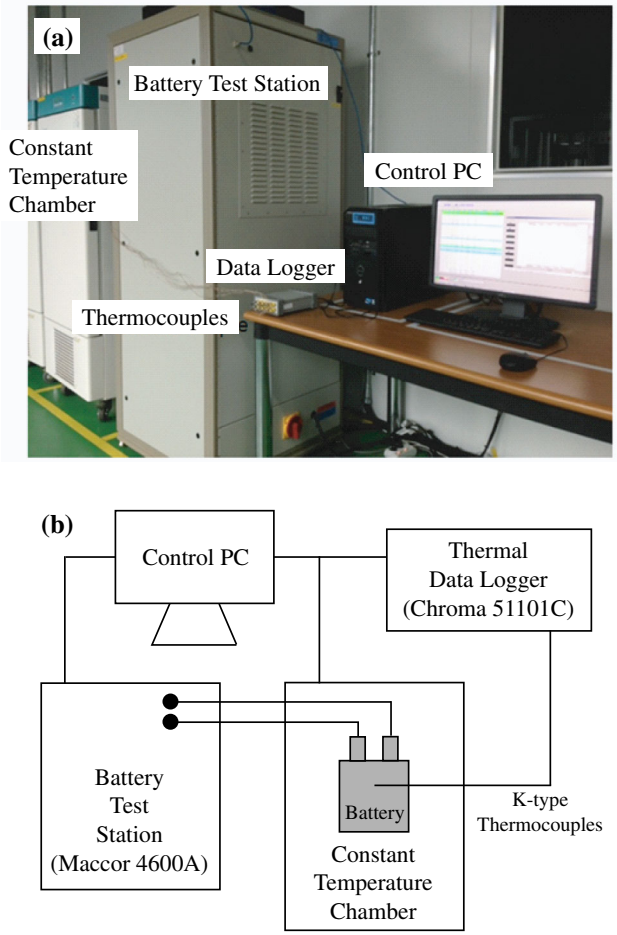

Fig. 2 **a** Schematic diagram of experimental setup and **b** picture of experimental devices

$$\rho C_P \frac{\partial T}{\partial t} = \nabla(\kappa \nabla T) + \dot{q} \tag{1}$$

where ρ is the density, C_p is the heat capacity, T is the temperature, t is the time, and κ is the thermal conductivity. $\dot{q}$ is the heat source per unit volume in the battery which is $\frac{\mathrm{d}\dot{Q}}{\mathrm{d}v}$. The heat source $\dot{Q}$ as derived by Thomas and Newman [5] is expressed as

$$\dot{Q} = I(V^o - V) - IT\frac{\partial V^o}{\partial T} - \sum_i \Delta H_i^{avg} r_i - \int \sum_j \left(\bar{H}_j - \bar{H}_j^{avg}\right) \frac{\partial c_j}{\partial t} \mathrm{d}\upsilon \tag{2}$$

where I is the applied current (which is positive on discharge and negative on charge), V is the cell voltage, V^o is the open circuit voltage (OCV), ΔH_i is the enthalpy change of chemical reaction i, r_i is the rate of reaction i, $\bar{H}_j$ is the enthalpy of species j, c_j is the concentration of species j, and υ is the volume. The first term on the right side of Eq. (2) is the heat generation due to irreversible resistance. Therefore, the first term can be written as I^2R_i [7, 8]. The

second term is the heat generation due to a reversible entropy change by recalling $IT\frac{\partial V^o}{\partial T} = T\Delta S\frac{I}{nF}$. This term can be either positive or negative, depending on the entropy change and the direction of the current. The third term is the heat generation due to a chemical reaction that may be present in the cell. The fourth term is the heat of mixing due to a concentration gradient in the electrodes. In this study, the last two terms were not considered by assuming that the side reactions accounting for aging are very slow and the concentration gradient within the electrodes are negligibly small [5, 11]. Therefore Eq. (2) can be reduced to

$$\dot{Q} = I^2R_i - IT\frac{\partial V^o}{\partial T} \tag{3}$$

Resistive heating is caused by the electrical resistance of the components to the passage of current. Therefore the first term mostly occur at the positive and negative current collectors (Al and Cu foils), and the positive and negative tabs. The second term mainly occurs at the positive and negative electrodes due to chemical reaction which is called the entropy change. The open circuit voltage (OCV) experiment at various temperatures gives the value of $\frac{\partial V^o}{\partial T}$. Therefore Eq. (3) can be written as

$$\dot{Q} = I^2R_{PCC} + I^2R_{NCC} + I^2R_{+tab} + I^2R_{-tab} - IT\left(\frac{\partial V^o}{\partial T}\right)_{PE} - IT\left(\frac{\partial V^o}{\partial T}\right)_{NE} \tag{4}$$

Using Eq. (4), the energy balance [Eq. (1)] allows us to solve heat source terms directly using Eq. (4), which does not include complex electrochemical processes. Since a coupling with the electrochemical-thermal model is not necessary in this model, computational cost can be reduced significantly, and thermal modeling of a complex three-dimensional structure can be achieved. This methodology allows simplification of the thermal modeling of a Li-ion battery in terms of thermal management.

3.2 Coupled thermal-electrical analysis

This study employed the FEA using ABAQUS to determine the resistive heating. In this software, the electrical current is solved using Ohm's law as follows.

$$i = -\sigma_i\nabla\varphi \tag{5}$$

where σ is the electrical conductivity, and φ is the electrical potential. The electrical potential in a steady flow of current is governed by the Laplace equation $\nabla^2\varphi = 0$. Therefore, the electrical potential and current density are obtained by electrical conduction analysis [18]. Using Ohm's law, the heat generation due to irreversible resistance is calculated as

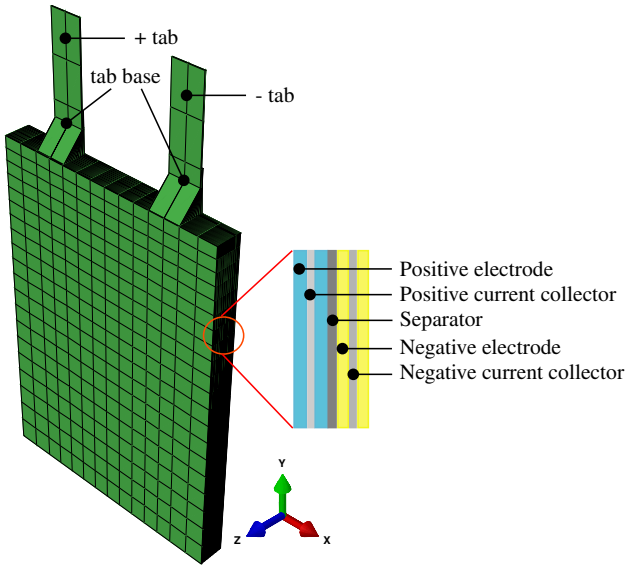

Fig. 3 Schematic configuration of a pouch type Li-ion battery model and finite elements meshes. The three-dimensional model consists of multiple layers of same repeating unit of positive electrode, positive current collector, separator, negative electrode, and negative current collector

$$i^2R_i = \int_{\upsilon} \nabla\delta\varphi \cdot \sigma_i \cdot \nabla\varphi d\upsilon \tag{6}$$

where υ is the volume. Since the electrical conductivity of the electrodes are very small, the electrical current at positive and negative electrodes can be neglected. A detailed description of the equations can be found in the Abaqus Analysis User's Manual [19].

3.3 Geometry and boundary conditions

A schematic configuration of the pouch-type Li-ion battery and finite element mesh considered in this study are shown in Fig. 3. The three-dimensional model is constructed using heat transfer solid elements. The finite element mesh has 25584 hexahedral elements and 29166 nodal points. The pouch cell is stacked by the same repeating units (positive electrode, positive current collector, separator, negative electrode, and negative current collector). The width and length of electrodes and current collectors are assumed to be same as 29.5 mm × 42 mm for the simplicity of the model. Table 1 lists geometry details, and properties that were collected from the literature [20–23]. The effect of the aluminum pouch on the thermal analysis is neglected because its size is too small to be considered. Although potential gradients are expected in the electrodes, the current generation is treated as uniform throughout the electrodes because thin electrodes are used. Thus, the potential gradient is negligibly small and the current flows quickly though the current collectors.

Table 1 Physical properties used for the transient thermal model

	Material	L (μm)	ρ (kg m^{-3})	κ (W m^{-1} K^{-1})	C_p (J kg^{-1} K^{-1})	σ (S m^{-1})
Positive electrode	$LiMn_2O_4$	57.5	4,140	5	0.7	0.069
Negative electrode	LiC_6	55	2,500	5	0.7	100
Positive current collector	Al	15	2,700	200	0.87	38×10^6
Negative current collector	Cu	10	9,000	380	0.381	60×10^6
Separator	PE	16	1,200	1	0.7	–
Positive tab	Al	100	2,700	200	0.87	38×10^6
Negative tab	Ni	100	8,910	91	0.26	14×10^6

To calculate the coupled thermal-electrical model, the discharge current is applied at the end of positive tab and the interface of negative electrode/negative current collector. During discharge, current flows from the anode to the cathode. Since the lead wire is not modeled in this study, discharge current is applied at these two points. The reference potential of zero is taken at the end of negative tab and the interface of positive electrode/positive current collector. In the case of charge, the reverse boundary conditions are applied. To solve the energy equation, convective heat transfer boundary conditions are applied to the outer surfaces. A surface boundary condition that is dependent on the convective heat transfer is expressed as

$$\dot{q}_{\text{convection}} = h(T - T_o) \tag{7}$$

where h is the heat transfer coefficient. The battery is operated at a constant temperature of 24.5 °C with heat transfer coefficient of 7.17 W m^{-2} K^{-1} [24].

Figure 4 shows the measured $\frac{\partial V^o}{\partial T}$ and the OCV of the LMO and LiC_6 considered in this study. $\frac{\partial V^o}{\partial T}$ is taken from Thomas et al. [25] and Srinivasan and Wang [6]. Because $\frac{\partial V^o}{\partial T}$ varies according to the Li content, the values of the Li content are obtained through the porous electrode model using the existing Li-ion battery model in the COMSOL Multiphysics with the Chemical Engineering Module. At the end of the discharge/charge cycles, the Li contents at the positive and negative electrode surfaces are calculated using the following equations.

$$x = \frac{c_1}{c_{1,\text{cathode}}^{\max}}, \quad y = \frac{c_1}{c_{1,\text{anode}}^{\max}} \tag{8}$$

where c_1 is estimated by taking the average of the Li-ion concentration at the particle surfaces. The initial Li compositions on the positive and negative electrodes are set to 0.3 and 0.75 for discharge and 0.8 and 0.1 for charge, respectively. The governing equations and constitutive equations used in this software package can be found in the literature [26–28], and in the COMSOL Multiphysics User's Guide [29]. For the sake of brevity, these equations will not be repeated in this paper. The parameters used in this model are listed in Table 2, and are taken either from measurement or the literature [15, 30, 31].

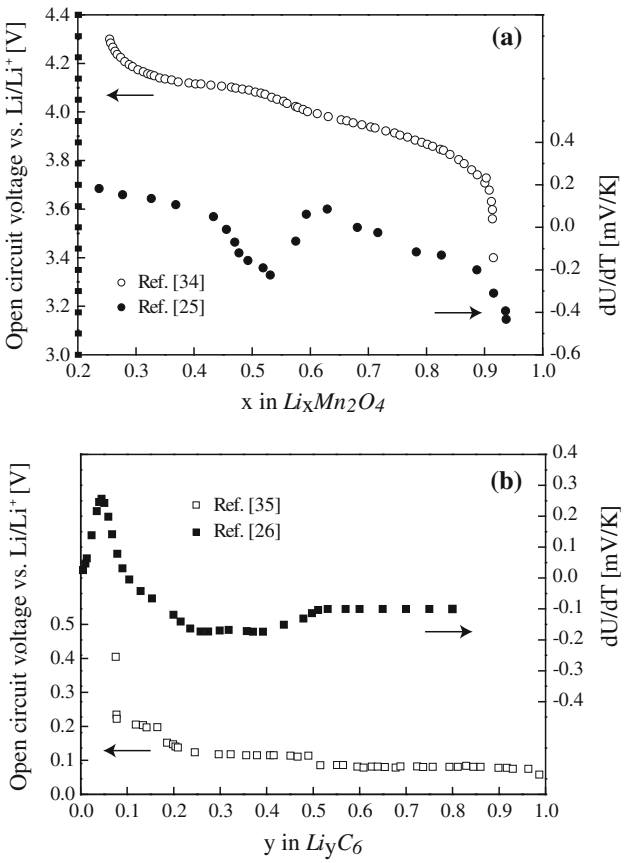

Fig. 4 Figure 3 open circuit voltage vs Li/Li$^+$ and entropy changes as a function of Li content in **a** LMO (x) and **b** LiC_6 (y)

3.4 Numerical procedure

A FEM based on the commercial finite element solver ABAQUS is used to solve the fully coupled governing equations. Governing equations for the constitutive equation of electrical flow (i.e., Ohm's law) and the thermal energy balance are solved in the same step by applying the same interpolation function. Using the obtained Li content and run-time, the transient thermal model employing the coupled thermal-electrical model is simulated. Because the thermal-electrical equations are unsymmetric, the unsymmetric solver is invoked automatically. The time increment for a constant-current discharge and charge is 1 s. The

Table 2 Parameters used to calculate the capacity characteristic

	Cathode	Anode	Separator
D_1 ($m^2\ s^{-1}$)	7.51×10^{-14}	3.9×10^{-14}	–
D_2 ($m^2\ s^{-1}$)	$1 \times 10^{-4} 10^{-4.43(54.0/(T-229.0-0.05c))} - 2.2 \times 10 - 4c_2$		
r_p (μm)	8	10	–
ε_1	0.62	0.508	–
ε_2	0.357	0.46	0.7
v	$0.601 - 0.24\sqrt{10^{-3}c_2} + 0.982\left[1 - 0.0052(T - 294.0)\sqrt{10^{-9}c_2^3}\right]$		
c_1^{max} ($mol\ m^{-3}$)	22,860	26,390	–
k ($(A\ m^{-2}\ mol\ m^{-3})^{3/2}$)	6.1×10^{-6}	4.85×10^{-6}	–

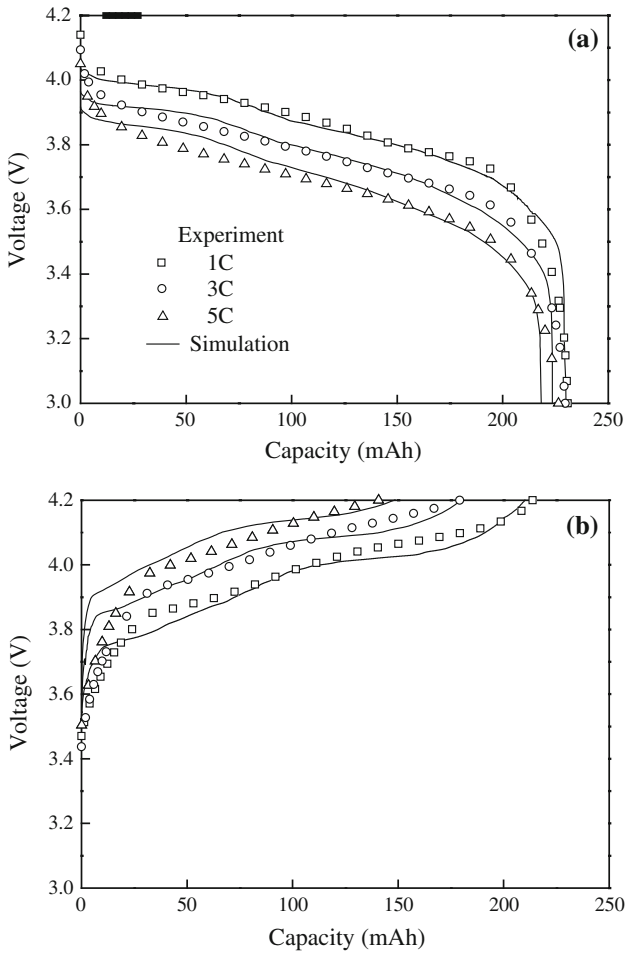

Fig. 5 **a** Discharge and **b** charge capacity at 1C, 3C and 5C rates. The simulation is compared with experiment

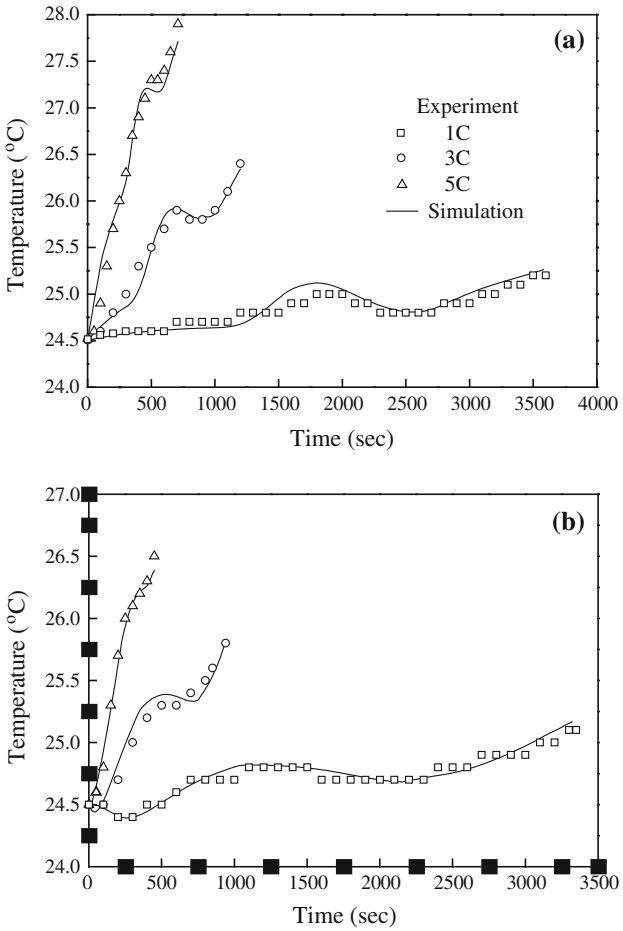

Fig. 6 **a** Surface temperature profiles at 1C, 3C and 5C rates **a** discharge and **b** charge. Temperature is measured at the center of the cell. The modeling results are compared with experimental results for the validation of thermal model

explicitly coded program is developed to calculate the heat source due to an entropy change. The computational time for the present calculation required about 25 s per time step on 12 nodes parallel processors with a 3.30 GHz clock speed.

4 Model validation

To validate the thermal model, a comparison between the experimental results and the FEA results is made. To examine the dynamic response of the thermal behavior,

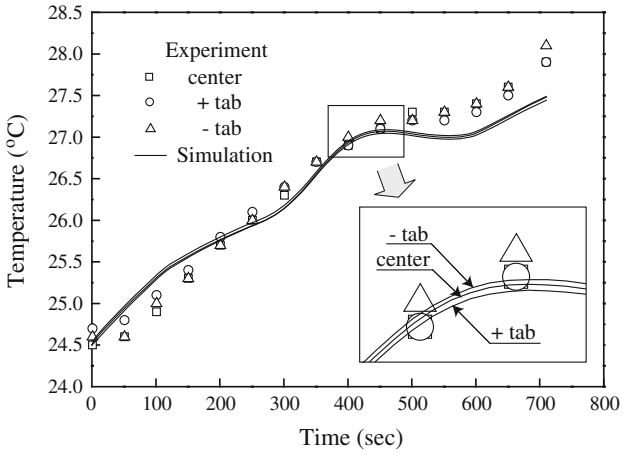

Fig. 7 Surface temperature profiles at 5C discharge. Temperatures of modeling and experiment are compared at three different locations. (positive tab base, negative tab base and center of the cell)

temperature profiles under various discharge and charge rates are presented in Figs. 5, 6, and 7. A comparison with the existing correlation is made at approximately the same locations.

4.1 Capacity validation

The capacity characteristic is first validated to identify the performance of the cell using COMSOL Multiphysics. Figure 5 shows the capacity characteristics of a pouch-type Li-ion battery. The discharge and charge capacity are predicted at rates of 1C, 3C, and 5C. The simulation results are in good agreement with the experimental measurements over various rates of discharge and charge. On the other hand, there is a slight discrepancy between the experiment and modeling in some regions. Because the simulation is conducted using a pseudo two-dimensional model by assuming constant parameters, this model is unable to predict the physics of the system accurately. Extending the model to three dimensions and the use of variable parameters that depend on the temperature might improve the accuracy, but this is beyond the scope of this work.

4.2 Thermal characteristic

To validate the thermal characteristic of a pouch-type Li-ion battery, the predicted temperature is compared with experimental data as shown in Fig. 6. The figure gives the experimentally and numerically obtained temperature profiles during discharge and charge. Figure 6a shows the surface temperature profiles at discharge rates of 1C, 3C, and 5C. The temperature is measured at the center of the cell. The temperature increase is small at the 1C discharge, whereas it is significant at the 5C discharge. As the discharge proceeds, the temperature increases while waving in the middle. This behavior is attributed to the chemical heat source, which is characterized by heat generation due to a reversible entropy change. From Fig. 4, $\frac{\partial V^o}{\partial T}$ has positive values at $0.6 < x < 0.7$ and $x < 0.46$ which means an endothermic process, and a steep gradient is observed at $0.46 < x < 0.6$. Thomas et al. [25] reported that $\frac{\partial V^o}{\partial T}$ changes from positive when the lattice is nearly empty, and to negative when next-nearest neighbor sites are nearly full. When $x < 0.4$, there is little ordering between the sublattices and each increment of lithium added to the lattice involves a similar interaction among neighbors. Monte Carlo calculations [32, 33] predicted strong ordering of lithium between the two lattices where the disorder-to-order transition occurs at $x \approx 0.4$, and order-to-disorder transition occurs at $x \approx 0.6$. Therefore, the almost constant entropy change at $x < 0.46$ results in a moderate temperature rise at the beginning of discharge, and a steep entropy change gradient made a waving region in the middle of the discharge. On the other hand, the peak and valley in the waving region become small at a high discharge rate. This indicates that the effect of heat generation due to a reversible entropy change becomes insignificant at a high discharge rate. This is because the heat sources are strongly dependent on the current density; i.e., $\dot{q}_{\text{resistance}} \sim i^2$ and $\dot{q}_{\text{entropy}} \sim i$, as can be seen in Eq. (3). Figure 6b shows the surface temperature profiles at charge rates of 1C, 3C, and 5C. The measuring point is the center of the cell. The surface temperature increases as the charge proceeds. Similar to the discharge curve, a waving region is observed in the middle. This is attributed to the heat generation due to reversible entropy change as previously discussed. At a charge of 1C, the temperature increase is small and the temperature profile fluctuates at the beginning. This is because of positive $\frac{\partial V^o}{\partial T}$ at $0.6 < x < 0.7$. On the other hand, at a 5C charge, the surface temperature increases significantly and the profiles become linear. As shown in Fig. 6a and b, the temperature profiles of the discharge and charge are different. The surface temperature on discharge is higher than that on charge at the end of the discharge/charge. The temperature difference becomes significant as the C rates increases. This is attributed to the entropy change which contributes differently on the discharge/charge cycle, and shorter charge time.

Figure 7 shows the surface temperature profiles at a 5C discharge. The simulated temperature is compared with experimental data at several measuring points. The surface temperatures are measured at the positive tab base, negative tab base, and the center of the cell. The temperature differences among the measured points are small which indicates a uniform temperature distribution. The negative tab base presents higher temperature, whereas the positive tab base presents lower temperature. This is attributed to

the different electrical conductivities between the two tabs. Because aluminum is used as a positive tab and nickel is used as a negative tab, higher resisting heat generation occurs at the negative tab base. Although the surface temperature is measured at various discharge and charge rates, these results are not presented because the temperature differences among the measured points are very small at a lower C rate which is hard to figure out.

The temperature profiles of the FEA result are in good agreement with the experimental results, and there is a small discrepancy between them. The slight difference between the FEA and the experimental results can be attributed to several causes. One reason is that the location of the thermocouples does not exactly match the locations of the FEA node. Another reason is that the value of entropy change used in this simulation might have an inaccuracy. As Thomas et al. [25] pointed out, although several experiments for the measurement of $\frac{\partial V^o}{\partial T}$ have been conducted, there is a discrepancy between their results depending on the measuring technique and the measuring error. Also, the material properties during operation can be changed due to a change in temperature. If the model parameters that depend on temperature can be used to update the material properties, more accuracy can be achieved. Moreover, coupling of the electrochemical-thermal model might improve the accuracy, but this is beyond the scope of this work.

5 Results and discussion

Current density and temperature distributions are obtained using the FEM-based commercial software. To investigate the uniformity of the current density and temperature that affects the cycle life and battery safety, these contours are illustrated in Figs. 8, 9, 10, and 11. The distributions of current density and temperature are presented at various discharge/charge rates.

Figure 8 shows the current density distribution at the end of a 5C discharge. Figure 8a and b show the current density distribution on the positive current collector and negative current collector, respectively. The current density near both tab bases is significantly higher than in the other locations, which corresponds to the results of Kwon et al. [9]. This is because most of the current flows through the small area of the tab base and the resulting large resistance. The simulation result reveals that the current density is asymmetrically distributed because of the different electrical conductivities of the two current collectors, even though the two tabs are symmetrically located. Kwon et al. [9] reported that the width of the tab base and the position of the two tabs significantly affect the current density distribution, and can affect the use of the active material of the electrodes. This indicates that the wide tab is favorable for the battery cycle life. On the other hand, a wide tab might cause difficulty in the manufacturing process and increase the possibility of electrolyte leakage through the interface of the tab and pouch.

The current density distribution on the positive current collector and negative current collector at the end of the 5C charge are shown in Fig. 9a and b. This figure presents a contour similar to that shown in Fig. 8, which indicates that the current density distribution on the discharge and charge are almost the same. This occurs because the applied current is the same, and has a different flow direction between discharge and charge. These results are in good agreement with the results of Kim et al. [10, 13]. The current density distribution at 1C, 3C, and 5C discharges/charges shows a similar contour, and gives only different values of current density. Therefore, these results are not presented in this work.

Figure 10a, b, and c show the temperature distribution of the pouch-type Li-ion battery at the end of 1C, 3C, and 5C discharges, respectively. The temperature distributions present different contours at each C rate, and are asymmetric due to the difference in electrical conductivities of the positive and negative tabs. The maximum temperature is found below the center of the cell on 1C discharge, at the center of the cell on 3C discharge, and at the negative tab base on 5C discharge. This is attributed to the applied current and different electrical conductivities of the two tabs. At a low C rate, the resisting heat generations at the current collectors and tabs are small because the applied current is low; i.e., nominal capacity is small. On the other hand, at a high C rate where high current is applied, the contribution of resisting heat generation becomes significant because of $\dot{q}_{\text{resistance}} \sim i^2$. Also the electrical conductivity of the negative tab is lower than that of the positive tab, which indicates higher heat generation at the negative tab. Therefore, the maximum temperature is observed at the negative tab base at 5C discharge. This is contrary to the results of Xiao Choe [16] and Yi et al. [17], who reported a higher temperature distribution near the positive tab. This is because they used copper on the negative tab with a higher electrical conductivity than that of the positive tab, which resulted in lower heat generation on the negative tab. On the other hand, precautions should be used when copper is used as a negative tab because copper is susceptible to corrosion when exposed to air. Also, copper is known to have problems in the process of resistance welding between the negative tab and negative current collector due to low electrical resistance. Nevertheless, the temperature differences across the cell are not significant, which indicates a uniform temperature distribution. This

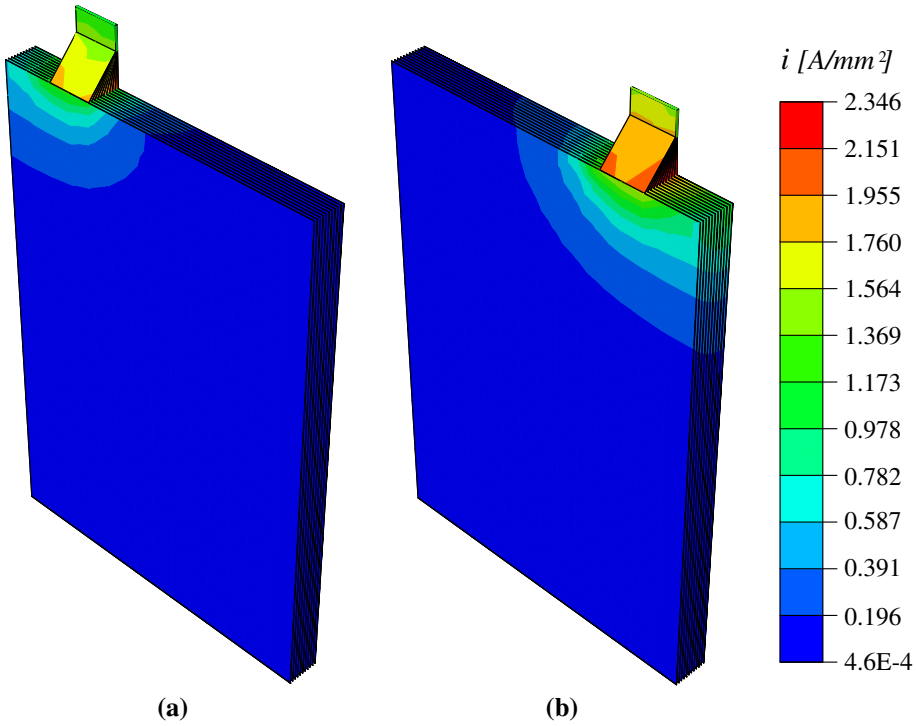

Fig. 8 Current density distribution at the end of 5C discharge. **a** positive current collector, **b** negative current collector

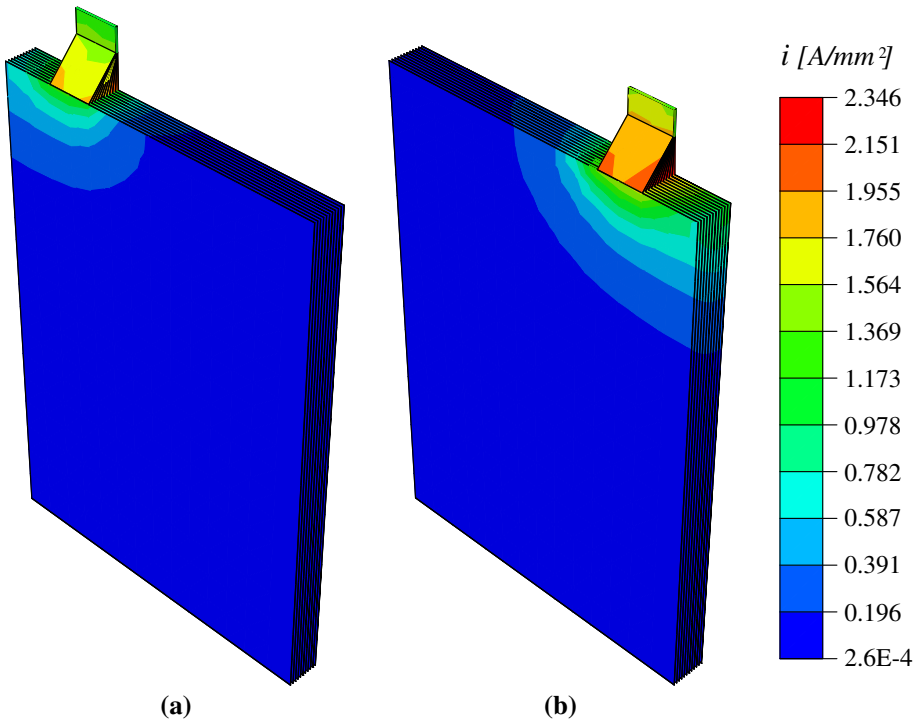

Fig. 9 Current density distribution at the end of 5C charge. **a** positive current collector, **b** negative current collector

small temperature differences are attributed to the small pouch cell and low nominal capacity.

Figure 11a, b, and c show the temperature distribution of the pouch-type Li-ion battery at the end of 1C, 3C, and 5C charges, respectively. The temperature distribution on charge has a similar contour to that on discharge. At 1C charge, a maximum temperature is observed on the same discharge location, which is located below the center of the cell. On the other hand, a maximum temperature is slightly displaced from the center of the cell toward the negative tab at 3C charge. At 5C charge, a maximum temperature is found on the same discharge location, but the overall

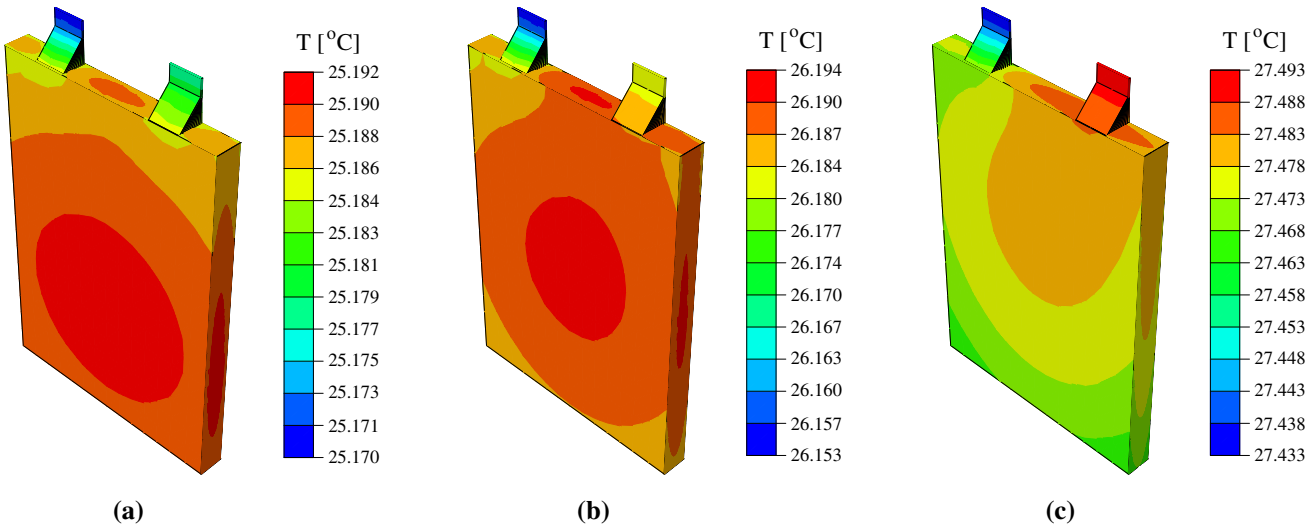

Fig. 10 Temperature distribution of pouch cell at the end of **a** 1C, **b** 3C and **c** 5C discharges

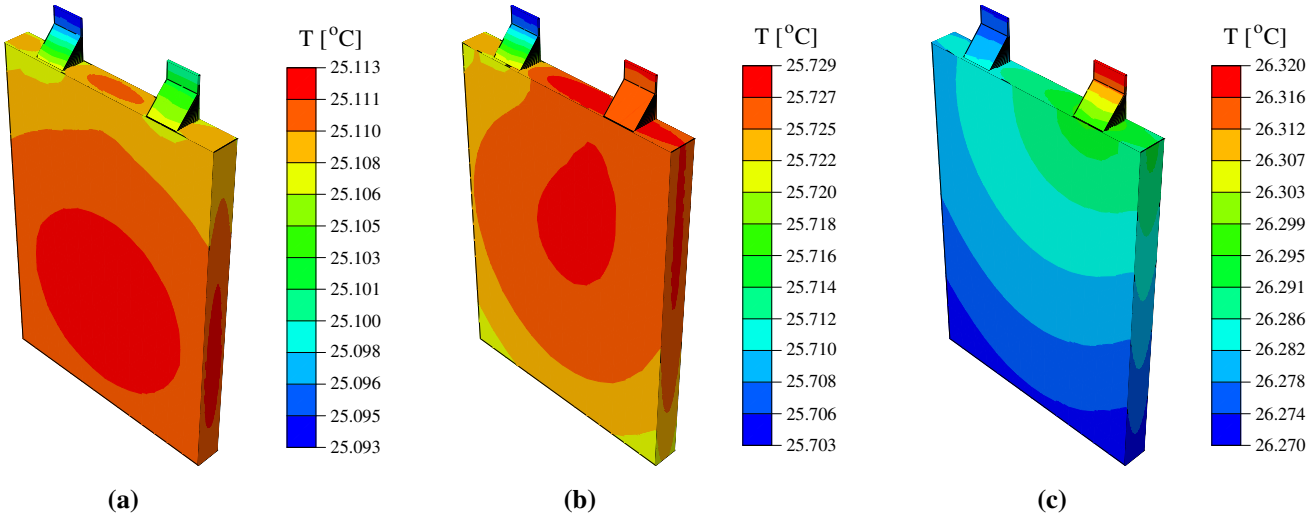

Fig. 11 Temperature distribution of pouch cell at the end of **a** 1C, **b** 3C, and **c** 5C charges

temperature distribution is slightly changed due to a comparatively higher temperature at the negative tab base. Furthermore the temperature range is changed, which is lower than the discharge temperature.

6 Conclusion

An FEM-based three-dimensional thermal model was developed to characterize the thermal behavior of a pouch-type Li-ion battery. A comparison of modeling and experimentally determined temperature profile results shows that the modeling results are in good agreement with the experimental data. These results suggest that the discharge temperature is higher than the charge temperature at the end of the discharge/charge cycle. The temperature profiles have a waving region, which is closely related to the entropy changes of LMO and LiC_6. On the other hand, the peak and valley in the waving region become smaller as the C rate increases. This indicates that the contribution of the entropy change is significant at a low C rate, whereas this becomes small at a high C rate. Also, this implies that thermal behavior is closely related to the entropy change and applied current. An asymmetric current density distribution is observed on the current collectors and high current density is found near the tab base. This is attributed to the different electrical conductivities of the two current collectors and the narrow tab base, which causes large resistances in this region. The temperature distributions are different at various C rates, but the temperature distributions of discharge and charge present similar contours at the same C rate. The maximum temperature is observed

below the center of the cell at the 1C rate, but it is located on the negative tab base at the 5C rate. This indicates that the effect of resisting heat generation by the negative tab is significant at a high C rate.

The results show that thermal model presented in this study is valid for various discharge/charge rates and can accurately predict the thermal behavior of a pouch-type Li-ion battery. Because the coupling of a complex electrochemical-thermal model is computationally expensive, the proposed model can be effective in predicting the cell temperature for thermal management. Moreover, by saving calculation costs efficiently, this model can be readily extended to the thermal analysis of a battery module or pack, which is necessary in EV and HEV battery design.

Acknowledgments This work was supported by the Dongguk University Research Fund of 2012.

References

1. Bernardi D, Pawlikowski E, Newman J (1985) A general energy balance for battery systems. J Electrochem Soc 132:5–12
2. Chen Y, Evans J (1993) Heat transfer phenomena in lithium polymer-electrolyte batteries for electric vehicle application. J Electrochem Soc 140:1833–1838
3. Newman J, Tiedemann W (1995) Temperature rise in a battery module with constant heat generation. J Electrochem Soc 142:1054–1057
4. Pals C, Newman J (1995) Thermal modeling of the lithium/polymer battery. J Electrochem Soc 142:3274–3281
5. Thomas K, Newman J (2003) Thermal modeling of porous insertion electrodes. J Electrochem Soc 150:A176–A192
6. Srinivasan V, Wang CY (2003) Analysis of electrochemical and thermal behavior of li-ion cells. J Electrochem Soc 150:A98–A106
7. Onda K, Kameyama H, Hanamoto T, Ito K (2003) Experimental study on heat generation behavior of small lithium-ion secondary batteries. J Electrochem Soc 150:A285–A291
8. Inui Y, Kobayashi Y, Watanabe Y, Watase Y, Kitamura Y (2007) Simulation of temperature distribution in cylindrical and prismatic lithium ion secondary batteries. Energy Convers Manag 48:2103–2109
9. Kwon KH, Shin CB, Kang TH, Kim CS (2006) A two-dimensional modeling of a lithium-polymer battery. J Power Sources 163:151–157
10. Kim US, Shin CB, Kim CS (2008) Effect of electrode configuration on the thermal behavior of a lithium-polymer battery. J Power Sources 180:909–916
11. Forgez C, Vinh Do D, Friedrich G, Morcrette M, Delacourt C (2010) Thermal modeling of a cylindrical LiFePO4/graphite lithium-ion battery. J Power Sources 195:2961–2968
12. Jeon DH, Baek SM (2011) Thermal modeling of cylindrical lithium ion battery during discharge cycle. Energy Convers Manag 52:2973–2981
13. Kim US, Yi J, Shin CB, Han T, Park S (2011) Modelling the thermal behavior of a lithium-ion battery during charge. J Power Sources 196:5115–5121
14. Kim GH, Smith K, Kim KJ, Santhanagopalan S, Pesaran A (2011) Multi-domain modeling of lithium-ion batteries encompassing multi-physics in varied length scales. J Electrochem Soc 158:A955–A969
15. Ye Y, Shi Y, Cai N, Lee J, He X (2012) Electro-thermal modeling and experimental validation for lithium ion battery. J Power Sources 199:227–238
16. Xiao M, Choe SY (2012) Dynamic modeling and analysis of a pouch type LiMn2O4/carbon high power Li-polymer battery based on electrochemical-thermal principles. J Power Sources 218:357–367
17. Yi J, Kim US, Shin CB, Han T, Park S (2013) Three-dimensional Thermal Modeling of a lithium-ion battery considering the combined effects of the electrical and thermal contact resistances between current collecting tab and lead wire. J Electrochem Soc 160:A437–A443
18. Wang BJ, Hilali SY (1995) Electrical-thermal modeling using ABAQUS. 1995 ABAQUS user's conference, Paris, pp 771–785
19. ABAQUS Analysis User's Manual, Version 6.10 (2010) Dassault Systemes Simulia Corp, Providence, RI
20. Doyle M, Newman J, Gozdz A, Tarascon JM (1996) Comparison of modeling predictions with experimental data from plastic lithium ion cells. J Electrochem Soc 143:1890–1903
21. Baker D, Verbrugge M (1999) Temperature and current distribution in thin-film batteries. J Electrochem Soc 146:2413–2424
22. Yue H, Huang X, Lv D, Yang Y (2009) Hydrothermal synthesis of LiMn2O4/C composite as a cathode for rechargeable lithium-ion battery with excellent rate capability. Electrochim Acta 54:5363–5367
23. Perry RH, Green DW (1997) Perry's Chemical Engineers' Handbook, 7th edn. McGraw Hill, New York
24. Holman JP (1986) Heat transfer, 6th edn. McGraw-Hill, Singapore
25. Thomas KE, Bogatu C, Newman J (2001) Measurement of the entropy of reaction as a function of state of charge in doped and undoped lithium manganese oxide. J Electrochem Soc 148:A570–A575
26. Ramadass P, Haran B, White R, Popov B (2002) Capacity fade of Sony 18650 cells cycled at elevated temperatures: Part I. Cycling performance. J Power Sources 112:606–613
27. Ramadass P, Haran B, White R, Popov B (2003) Mathematical modeling of the capacity fade of Li-ion cells. J Power Sources 123:230–240
28. Ramadass P, Haran B, Gomadam PM, White R, Popov B (2004) Development of first principles capacity fade model for Li-ion cells. J Electrochem Soc 151:A196–A203
29. COMSOL Multyphisics User's Guide, Version 3.5a (2008) COMSOL AB
30. Valoen LO, Reimer JN (2005) Transport properties of $LiPF_6$-based Li-ion battery electrolyte. J Electrochem Soc 152:A882–A891
31. Albertus P, Christensen J, Newman J (2009) Experiments on and modeling of positive electrodes with multiple active materials for lithium-ion batteries. J Electrochem Soc 156:A606–A618
32. Darling R, Newman J (1999) Dynamic Monte Carlo simulations of diffusion in $Li_yMn_2O_4$. J Electrochem Soc 146:3765–3772
33. Kim SW, Pyun SI (2001) Thermodynamic and kinetic approaches to lithium intercalation into $Li_{1-\delta}Mn_2O_4$ electrode using Monte Carlo simulation. Electrochim Acta 46:987–997
34. Less GB, Seo JH, Han S, Sastry AM, Zausch J, Latz A, Schmidt S, Wieser C, Kehrwald D, Fell S (2012) Micro-scale modeling of Li-ion batteries: parameterization and validation. J Electrochem Soc 159:A697–A704
35. Ohzuku T, Iwakoshi Y, Sawai K (1993) Formation of lithium-graphite intercalation compounds in nonaqueous electrolytes and their application as a negative electrode for a lithium ion (shuttlecock) cell. J Electrochem Soc 140:2490–2498